DFT-assisted spectroscopic studies on the coordination of small ligands to palladium: from isolated ions to nanoparticles

Sebastiano Campisi,[a] Cameron Beevers,[b] Ali Nasrallah,[b] C. Richard A. Catlow,[b] Carine e. Chan-Thaw,[a] Maela Manzoli, Nikolaos Dimitratos, David J. Willock,[b] Alberto Roldan*,[b] Alberto Villa*,[a]

[a] Dipartimento di Chimica, Università degli Studi di Milano, via Golgi 19, I-20133Milano, Italy

[b] Cardiff Catalysis Institute, School of Chemistry, Cardiff University, Main Building, Park Place, CF10 3AT, Cardiff, United Kingdom.

[c] Department of Drug Science and Technology and NIS - Centre for Nanostructured Interfaces and Surfaces, University of Turin, Via P. Giuria 9, 10125 Turin, Italy.

[d] Dipartimento di Chimica Industriale e dei Materiali, ALMA MATER STUDIORUM Università di Bologna, Viale Risorgimento 4, 40136 Bologna, Italy

Abstract

A combination of experimental spectroscopies (UV-Vis. and FT-IR) and computational modelling was used to investigate the coordination of small ligands (aminopropanol and propanediol) to Pd species during metal nanoparticles formation process. Differences emerged between O- (propanediol) and N-containing (aminopropanol) ligands. In particular, a strong interaction between the NH amino group and Pd^{2+} ions could be inferred on the basis of spectroscopic evidences, which was corroborated by theoretical simulations, which confirmed the preferential coordination of aminopropanol through the NH group. This interaction seems to potentially cause the aminopropanol ligand to control the particle shape through a selective blocking of Pd(100) facets, which promote the growth on the Pd(111) facets.

Keywords: Pd, nanoparticles control, ligand, UV-Vis., FTIR, DFT

1. Introduction

In the last decades, metal nanoparticles have been used increasingly as key components for applications in several fields such as energy conversion and storage, biomedicine and life science, electronics, information technology and catalysis thanks to their unique and fascinating properties.[1–4] Most of the physicochemical properties of metal nanoparticles (MNPs) (e.g. optical, catalytic, magnetic and electronic properties) are highly dependent on a set of structural and morphological parameters, including composition, particle size, shape and exposure of facets, crystal structure, surface modification and environment. Despite this strong relationship between structure and function, the practical applications and the performances of MNPs are still limited by the lack of a clear predictability of the synthesis outcome in terms of size and morphological dispersion.[5,6]

Indeed, despite extensive studies and significant advances, the development of synthetic routes able to produce metal nanoparticles with an enhanced degree of compositional, dimensional, morphological and structural control still remains an open challenge. This difficulty arises, in part, from the significant number of factors affecting solution-based methods, which need to be considered and tuned in order to achieve rational design of size- and shape-controlled MNPs syntheses. The metal reduction potential, the nature and concentration of precursors, the reducing agent, the solvent, the temperature, and the mass transfer phenomena have a considerable impact on the mechanisms of nucleation and growth.[7–10] In addition, capping agents are commonly used in solution-phase synthesis to stabilize MNPs and to prevent their aggregation. The capping agents are often selected from various types of molecules, such as: thiols, amines, halides, carboxylic acids, phosphines, polymers and surfactants.[11–13] Capping agents can play multiple roles including providing colloidal stabilization and acting as structure directing agents.[7,11,14–19] Furthermore, as with conventional ligands, the capping agents can coordinate metal centres during different stages from metal precursors to metal nanoparticles. During the synthesis process, the metal

precursor is decomposed and reduced into metal atoms, which then aggregate and evolve towards the formation of clusters and then nanoparticles. The role of the capping agents in the overall thermodynamics and kinetics of the nucleation-growth processes derives from the different interactions with metal ions, MNPs and several intermediates, as shown by many experimental studies.[6,7,11,12,17,20,21] The concentration ratio of capping agent and metal has been demonstrated to affect the final sizes of alkanethiolate-capped Au NPs.[22] The interaction strength influences the particle size as reported by Karim *et al*. for Pd NPs synthesized in the presence of oleylamine (weak capping agent) or trioctylphosphine (strong capping agent).[23] The capping agent can also induce significant variations in the electrochemical reduction potential of metal ions, as suggested by the studies by Biacchi and Schaak concerning the effect of different polyols on the reduction of Rh salts.[24]

More recently, by combining *in-situ* small angle X-ray scattering (SAXS) and kinetic modelling, Mozaffari *et al.* investigated in detail the mechanisms of Pd NPs nucleation and growth.[25] The study demonstrated that, in different solvents (pyridine and toluene), the capping agents, acetate and trioctylphosphine (TOP), can exert a kinetic control on both the nucleation and growth rates, which was achieved by examining the concentration of kinetically active metal precursor and the number of free surface sites on the respective NPs' facets.

The capping agent not only influences the formation of MNPs, but can also irreversibly adsorb onto their surfaces affecting their performance and utility, which can drastically reduce the activity of heterogeneous catalysts.[26–28] It has been demonstrated that adsorbed capping agent molecules create an interphase, where diffusional, steric, and electronic effects can control and modify the overall activity and selectivity of catalytic reactions.[27] The reaction pathway is often governed by the preferential interactions between capping agent molecules and specific active sites (facets, edges, corners, defects) on the MNP surfaces.[28]

For these reasons, a significant amount of research has been devoted recently to investigate the connection between metal–capping agent interactions and the formation mechanisms of MNPs in solution, as well as the nature and role of the local ligand environment of metal species in solution. Several studies have been reported using advanced characterization techniques (e.g. SAXS, liquid cell TEM, and EXAFS) to provide a molecular level understanding of the roles of capping agents during the formation of metal NPs.[7,11,17,19–21,29–43] Here, we employ a combination of UV-Visible (UV-Vis.) and Fourier transform infrared (FT-IR) spectroscopies and Density Functional Theory (DFT) modelling to investigate the coordination of small ligands (diols and amino alcohols) to Pd^{2+} ions and Pd NPs. The complementary use of conventional spectroscopic techniques and theoretical modelling has already been demonstrated to be a powerful tool in investigating metal-ligand interactions in Au and Ag NPs.[34–36,40,44] The pH dependence of interaction strength and conformation of thiolate and thione molecules at the surface of Au NPs has been studied by means of surface-enhanced Raman spectroscopy (SERS) combined with DFT modelling by Ansar *et al.*[36] The synthesis of amidine-stabilized Ag NPs via hydrogenolysis of silver amidinate in the presence of hexadecylamine was explored by Cure *et al.* through nuclear magnetic resonance and SERS spectroscopies in combination with DFT simulations devoted to unravelling the coordination of ligands to Ag NPs.[40] Singh *et al.* monitored the synthesis of curcumin-capped Au NPs by *in situ* UV-Vis. spectroscopy and experimental results were correlated with DFT calculations exploring the formation of several complexes of curcumin with Au^{3+} ions in various conformational isomeric forms.[35] In this study, we focused on Pd NPs, which were selected as a model metal system due to their prevalence and relevance to heterogenous catalysis. DFT–derived spectra were used to interpret the experimental results in detail. Our results illustrate the DFT–assisted spectroscopic approach to describe the ligand coordination to NP's facets. The species present in the experimental reaction solutions have been examined through comparison of experimental with computed spectra.

2. Experimental

2.1 Synthesis of Pd NPs

Solid Na_2PdCl_4 (0.094 mmol of Pd) and aminopropanol or propanediol water solution (1 wt.%) (Pd/capping agent 1 : 100 weight ratio) were added to 100 mL of H_2O. After 3 min, $NaBH_4$ (Pd/NaBH4 = 1/8 mol/mol) solution was added to the yellow-brown solution under vigorous magnetic stirring. A brown Pd(0) sol was immediately formed.

2.2 Spectroscopic studies

UV–Vis. spectra of sols were recorded using a PERKIN ELMER λ25 spectrophotometer in H_2O between 190 and 1200 nm using a quartz cuvette. The samples were loaded into a rectangular quartz cuvette of one cm width and three cm height. The sample measurement was made with respect to a reference scan of the solvent (i.e., water) at controlled pH. Spectra were recorded after 10, 60, and 300 seconds from the addition of the capping agent.

FT-IR experiments were performed with cells allowing spectrum scanning on the liquid samples at room temperature. The FT-IR spectra were recorded using a Perkin Elmer 2000 spectrometer (equipped with a cryogenic MCT detector). The spectra were acquired in the 4000-1000 cm^{-1} range with a 2 cm^{-1} resolution. To collect the FT-IR spectra of our aqueous solutions, we employed a commercial demountable transmission cell equipped with CaF_2 windows (shown in Figure SI-1 of the supporting information). To collect the spectra, the solution is dropped onto a CaF_2 window and sandwiched with another equal window, such that no gas bubbles are trapped. This procedure implies that the amount of sample is very low and the contribution of the solvent is negligible.

The measured solution sample forms a thin liquid film between the two windows, which is typically less than 0.01 mm thick. It is not possible to measure the optical path, being that of the liquid film. Indeed,

as the thickness is not constant from measurement to measurement, this type of cell is unsuitable for quantitative analysis.

2.3 Computational details

This project uses Density Functional Theory (DFT) as incorporated within the ORCA[45] and VASP (Vienna Ab initio Software Package)[46–49] simulation codes to model precursor molecules and experimentally formed nanoparticles respectively; the latter of which is modelled as extended periodic surfaces. The Perdew-Burke-Ernzerhof (PBE) exchange-correlation functional[50,51] was employed to account for the exchange and correlation effects on formed NPs with the projector augmented-wave (PAW) method used to represent atomic core states.[52,53] To ensure consistency between periodic and non-periodic simulations, extended tests were carried out using PBE and Becke-Perdew-86 functional (BP86). These consistency tests have shown the PBE functional to be a reasonable compromise between cost and accuracy for second row transition metals modelled using both periodic and atom-centred DFT methodologies.[54] Dispersion effects were included in both atom-centred and plane-wave models using Grimme's empirical DFT-D3 model.[55] For non-periodic, atom centred models, DFT-D3BJ (DFT-D3 with Becke-Johnson damping) was used to prevent artificial short-range repulsive interactions.[55–58]

Dipole correction along the z-direction of the periodic slab model was applied in all calculations. A Monkhorst-Pack grid was used to sample the Brillouin zone.[59] For optimisation calculations, the number of *k*-points used was 7×7×7 for the optimisation of the fcc unit cell bulk structure, and 7×7×1 for the surfaces. For the adsorption calculations on the (111) surface, a 5 atomic layers thick slab with a *p*(4×4) surface supercell (80 atoms), was employed. For the (100) surface a *c*(3×3) surface slab was constructed, again 5 layers thick (90 atoms). During optimisation calculations, the top two layers of the slabs were relaxed and the lower 3 layers fixed at their optimised bulk positions. A 3×3×1 *k*-points sampling was

used for all surface calculations. The periodically repeated slabs were separated by a 20 Å vacuum layer along the Z direction, which is enough to avoid any spurious interaction with periodically replicated images. A kinetic energy of the plane waves was set to 400 eV ensuring no Pulay stress. The convergence criterion was set such that the calculations converge when the forces are less than 0.02 eV $Å^{-1}$ for adsorption calculations, 0.001 eV $Å^{-1}$ for the bulk, and 0.01 eV $Å^{-1}$ for surface optimisation calculations. The adsorption energy was computed using equation (1).

$$E_{ads} = (E_{ad+sl} - E_{sl} - E_{ad}) \qquad (1)$$

Where E_{ad+sl} is the energy of the adsorbate adsorbed on the slab, E_{sl} is the energy of the naked slab, and E_{ad} is the energy of the adsorbate in gas phase, i.e. in a cell large enough to avoid intermolecular interactions.

The ORCA implementation of Karlsruhe quadruple zeta with valence and polarisation functions basis set (def2-QZVP), the auxiliary Weigend basis set (def2/J), and Stuttgart–Dresden effective core potentials (ECPs) were used for all non-periodic atom-centred DFT calculations.[60–62] The convergence criteria for these calculations were an energy change of 2.72×10^{-5} eV with a maximum gradient of 5.14×10^{-3} eV $Å^{-1}$ and a maximum displacement of 5.29×10^{-4} Å. Analytical frequency calculations were also performed to optimise and confirm the geometry of the aminopropanol liganded molecular precursor.

The species present in the reaction solutions have been examined through comparison of experimental with computed spectra. Simulated UV-Vis. spectra were calculated using the simplified Tamm-Dancoff approximation of time-dependent DFT (sTDA-DFT), which has been shown to give good agreement with time-dependent DFT for the electronic transitions energies, although, it is known that intensities calculated using this method are less reliable.[63] The calculation efficiency of sTDA-DFT has also been

increased by employment of the RIJCOSX approximation of the Coulomb and exchange integrals. Structures showing sTDA-DFT transitions consistent with the wavelength of experimentally observed bands were also calculated using the more demanding time-dependent DFT (TD-DFT) with the RIJCOSX integral approximation. TD-DFT spectra were examined using the Multiwfn software package, which applies Gaussian curve broadening.[64] Calculated excitations and orbital compositions were determined using the Mulliken method.[65] Localised orbital centroid analysis was also undertaken in order to examine the ligand bonding and oxidation state of the Pd^{2+} ions in the nanoparticle precursor molecule using the methodology of Vidossich and Lledós.[66] This utilised the ORCA software package's implementation of the Pipek-Mezey population-localisation methodology to derive localised orbitals from the DFT-calculated electronic structure. [67] [68] The gas phase energy changes of reaction, ΔE_r, were calculated using equation 2.

$$\Delta E_r = \sum E_{products} - \sum E_{reactants} \qquad (2)$$

Results and discussion

The coordination of the capping agent to Pd^{2+} ions and Pd nanoparticles was investigated by UV-Vis. and FT-IR spectroscopies. 3-aminopropanol (AP) and 1,3-propanediol (PD) were studied as model capping agents for the Pd sol. These molecules were selected because their molecular structures resemble the repeating units of several polymers commonly used as capping agents for Pd NPs (e.g. poly vinyl alcohol, poly ethylene glycol, poly vinyl pirrolydone).

The coordination of the capping agent molecules to Pd^{2+} ions was monitored in real time by UV-Vis spectroscopy under typical synthetic environments for the generation of the Pd sol. The starting H_2PdCl_4 salt in solution (black line in figures 1, 2, and 3, which show observed and calculated spectra) is characterized by UV-vis. bands at 310 and 418 nm. These bands could be associated to ligand to metal

charge-transfer (CT) and *d–d* electronic transitions. Typically, bands originated from *d-d* transitions are much less intense and more resolved than CT transitions. On the other hand, the identification of the Pd species responsible for these spectral features is no trivial matter. As reported by Elding, the predominant species found in acidic media are $PdCl_4^{2-}$ and $[PdCl_3(H_2O)]^-$.[69] Spectroscopic evidences of the formation of these species were obtained also using solid $PdCl_2$ as precursor by Freund *et. al*, who collected UV-vis. spectra of solutions depending on the pH of the media.[70] At a pH of 1.3, *d–d* and charge transfer transitions at 280 nm/475 nm for $PdCl_4^{2-}$ and 320 nm/430 nm for $[PdCl_3(H_2O)]^-$, respectively, were observed. At a pH of 10, a spectrum showing increased background absorption was observed along with a rise at short wavelengths with a feature centered at 270 nm. In addition, Grogan and Nakamoto reported the formation of dimeric species. $Pd_2Cl_4(EthO)_2^{2-}$ which can be described as a Pd analogue to the Pt salt Zeise's dimer.[71]

To identify the contribution of each of these species to the experimental spectra Time-Dependent Density Functional Theory (TD-DFT) simulations were carried out to model UV-Vis. absorption spectra of $PdCl_4^{2-}$, $[PdCl_3(H_2O)]^-$ and $Pd_2Cl_6^{2-}$ species. TD-DFT computed UV-Vis. spectra of $PdCl_4^{2-}$ and $Pd_2Cl_6^{2-}$ (green and blue dotted curves in Fig.1, respectively) are in good agreement with the observed experimental spectrum (black curve in Fig. 1). The computed data for the chlorine bridged dimer indicate that the characteristic 420 nm band in the experimental spectra is due to a Cl *p*-Pd *s* transition. However, the breadth of this band is likely due to the contributions of a 470 nm transition, indicating a predominantly Pd *d* to Pd *p* excitation involving both palladium ions of the dimer, and a 388 nm transition observed in the computed spectrum of $PdCl_4^{2-}$, attributable to a predominantly *p-p* excitation from chlorine to palladium. Therefore, the experimental band centred at 418 nm could include all the contributions predicted by the model systems.

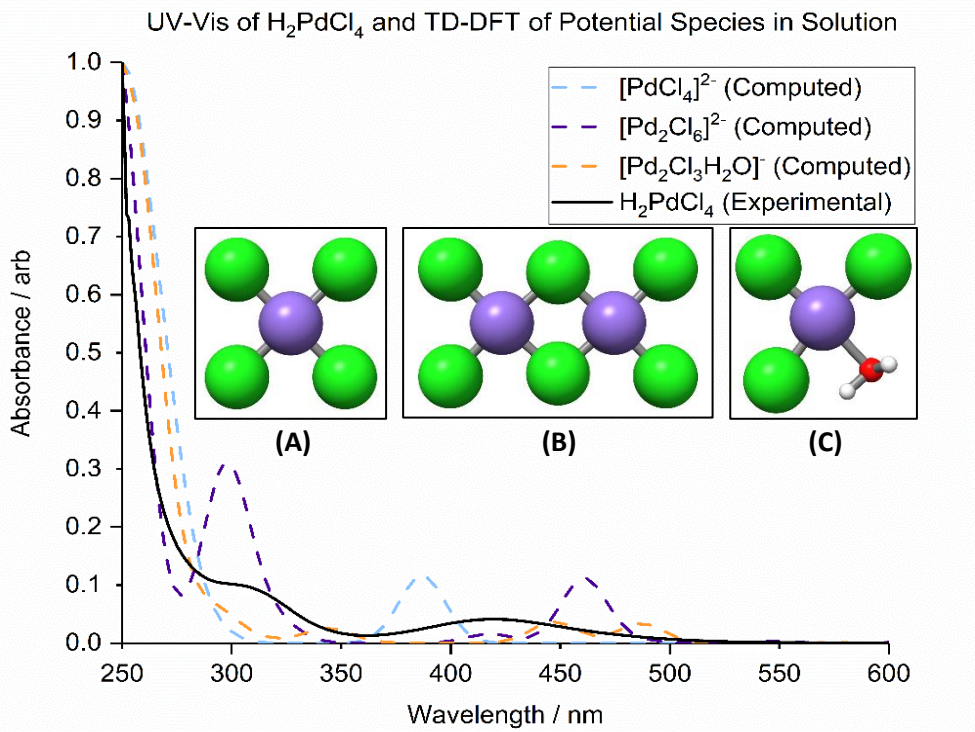

Figure 1: Experimental UV-Vis. spectra of H_2PdCl_4 in solution at pH 3 (black), computed UV-Vis. spectra of $[PdCl_4]^{2-}$, $[Pd_2Cl_6]^{2-}$, and $[PdCl_3H_2O]^-$. Inset: Structures of $PdCl_4^{2-}$, (A); $Pd_2Cl_6^{2-}$, (B); and $[PdCl_3(H_2O)]^-$, (C). Colour code: Pd: cyan; Cl: green; O: red and H: light grey.

The inherently large uncertainty in the relative intensities of bands obtained using the TD-DFT methodology means that the position of the peaks is to be used to analyse the spectra.[63] The broad band present at 425 nm is likely composed of a combination of peaks caused by contributions of the three computationally modelled structures. Furthermore, the shoulder observed in the experimental spectrum at 310 nm is consistent with the computed spectrum of the dimer shown in figure 1(B). The agreement of these computed excitations with experimental spectra suggests that the sol is comprised of an equilibrium mixture of $Pd_2Cl_6^{2-}$, $PdCl_4^{2-}$, and $[PdCl_3(H_2O)]^-$, The existence of these species is also supported by the calculation of the energies of reaction for the formation of $Pd_2Cl_6^{2-}$ and $[PdCl_3(H_2O)]^-$ from $PdCl_4^{2-}$, shown in Table 1. These values indicate that the formation of the dimer and the water containing complex are both exothermic processes with the dimer being the more energetically favourable.

Table 1: Energy change of reaction (ΔE_r) for the formation of $Pd_2Cl_6^{2-}$ and $[PdCl_3H_2O]^-$ from $PdCl_4$

Products	**ΔE_r / kJmol^{-1}**
$Pd_2Cl_6^{2-}$	-252
$[PdCl_3(H_2O)]^-$	-215

The addition of the capping agent to the Pd^{2+} solution in 1,3-propanediol led to no substantial changes in the observed spectrum (cyan dotted line vs. blue line in Figure 2). Conversely, upon reduction with $NaBH_4$ (red line), the band at 418 nm was not evident while an increased background absorption and a rise at short wavelengths with a maximum absorption at 285 nm were observed.

The observed increment in the background intensity can be attributed to the scattering induced by the formation of colloidal palladium particles and could be responsible for the masking/disappearance of the band at 418 nm. The blue shift of the CT band could be correlated to the increase of pH due to the $NaBH_4$ addition. However, the exact assignment of the observed band at 285 nm is still undetermined. According to Klasovsky *et al.* this peak relates to plasmon excitation in the colloidal particles.[69] However, Boily argued that it is also compatible with a charge-transfer transition of Pd chloro-hydroxo complexes, $PdCl_x(OH)_y^{n-}$, which are stable solution species under our experimental conditions, according to the hydrolysis equilibrium.[72]

The effect of adding the AP capping agent to the sol Pd^{2+} with the subsequent metal reduction is shown in figure 3. As expected, the initial UV-Vis. spectrum of Pd(II) (blue line) is consistent with that of figure 1, further pointing out the reproducibility of the experimental procedure. Upon addition of AP (green line), the broad band centred at 418 nm is depleted, and the decrease in intensity of the shoulder at 307 nm is accompanied by a broadening and a shift of the peak to 317 nm. These significant changes are a consequence of the chlorine ligand substitution by the AP capping agent.

These results are consistent with the computational analysis; the TD-DFT spectrum of the most favourable product, $[PdCl_3AP]^-$, (Figure 4, dashed blue line) was also found to be consistent with the experimental results. The energies of reaction for the formation of aminopropanol ligandated complexes

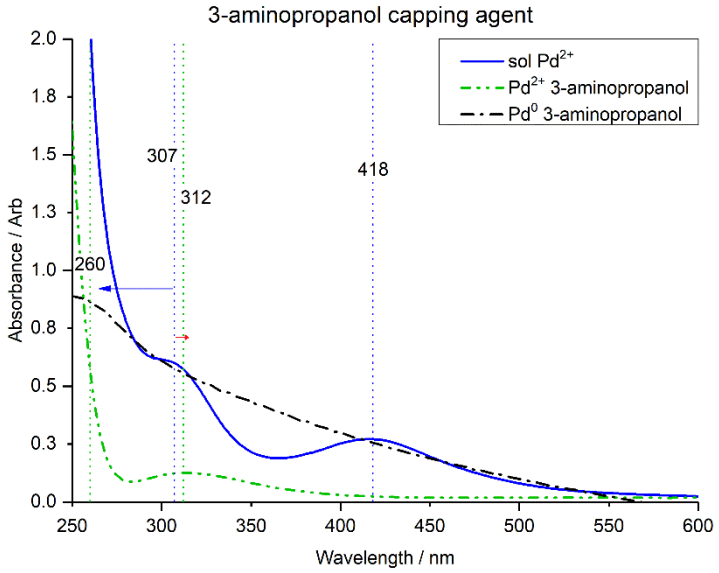

Figure 3: UV vis spectra of H_2PdCl_4 in solution (blue), in presence of the capping agent 3-aminopropanol (green), Pd with 3-aminopropanol reduced (black).

from $PdCl_4$ are shown in table 2.

Table 2: Energy change of reaction for the potential products of the reaction between $PdCl_4$ and 3-aminopropanol.

Potential Products	**ΔE_r / kJmol^{-1}**
$PdCl_2OHAp$ (cis)	-207
$PdCl_2OHAp$ (trans)	-188
$PdCl_3Ap$	-305
$PdCl_2Ap_2$	-295

The peak observed at 334 nm in the computational spectrum shows an excitation from a hybrid Pd *d* - Cl *p* orbital to a molecular orbital composed from the palladium *sp* and a hybridisation of orbitals in the aminopropanol ligand.

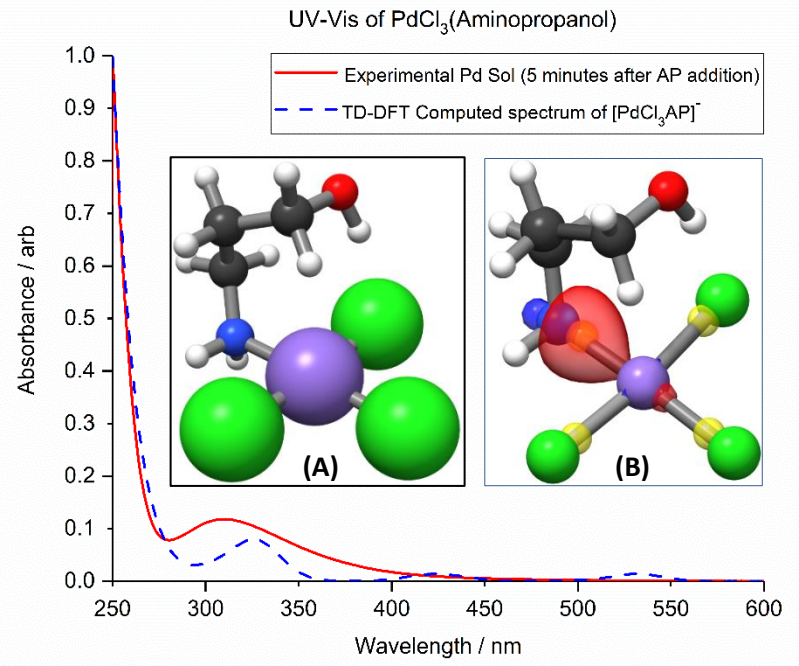

Figure 4: UV-Vis. spectra of $PdCl_4^{2-}$ sol in presence of the capping agent 3-aminopropanol (green) and computed TD-DFT spectrum of $PdCl_3AP$ (blue dashed). Inset: (A), $PdCl_3AP^{1-}$ lowest energy geometry; (B), $[PdCl_3Ap]^-$ with the Pd–N localised bonding orbital and the centroids for the Pd–N and Pd–Cl bonds. Colour code: Pd: lilac ; Cl: green; O: red ; N: blue; C: dark grey; H: white; and localised orbital centroids: translucent yellow.

This agreement with the experimental spectrum strongly suggests that the aminopropanol is directly attached to a Pd^{2+} species in a structure consistent with the computational predictions. A similar suggestion was reported by Groppo *et al.*[32] who compared the Diffuse Reflectance UV-Vis. spectra of bulk $Pd(OAc)_2$ diluted in SiO_2 and in pyridine. The bulk $Pd(OAc)_2$ in silica exhibited a band maximum

at 400 nm, whilst the one diluted in pyridine revealed a peak centered around 330 nm. As a possible explanation, the authors suggested that one or two acetate ligands were substituted by pyridine units.

This interaction between the NH group and the Pd^{2+} ions involves a strong interaction between the electron-rich amino group and the metal ion, which could induce a change in the actual oxidation state of the metal by partial reduction. For this reason, centroid analysis of the Pipek-Mezey localised orbitals was utilised to examine the oxidation state of Pd and the character of the AP−metal bond, figure 4 (B). The localised two-centred bonding orbitals indicated that the Pd−AP bond was largely dative in character with the electrons in the bonding orbital being biased towards the more electronegative nitrogen. Analysis of the single atom orbitals showed the electronic configuration of Pd atom to be consistent with Pd(II), $4s^2 4p^6 4d^8$, due to the presence of eight centroids centred upon the Pd atom and the bonding orbital centroids being biased towards the ligands. Coordination of the ligand does not therefore involve a redox process.

Upon reduction with $NaBH_4$, the UV-Vis. spectrum (Figure 3, red line) assumed a very broad profile, where it is difficult to uniquely identify defined features or any eventual shifts. A significant increase in the background absorbance was indeed observed, which, as in the case of 1,3-propanediol, was attributed to Willis-Tyndall scattering which is characteristic for the formation of particles.

In order to obtain more information on the coordination of 1,3-propanediol and 3-aminopropanol to Pd^{2+}

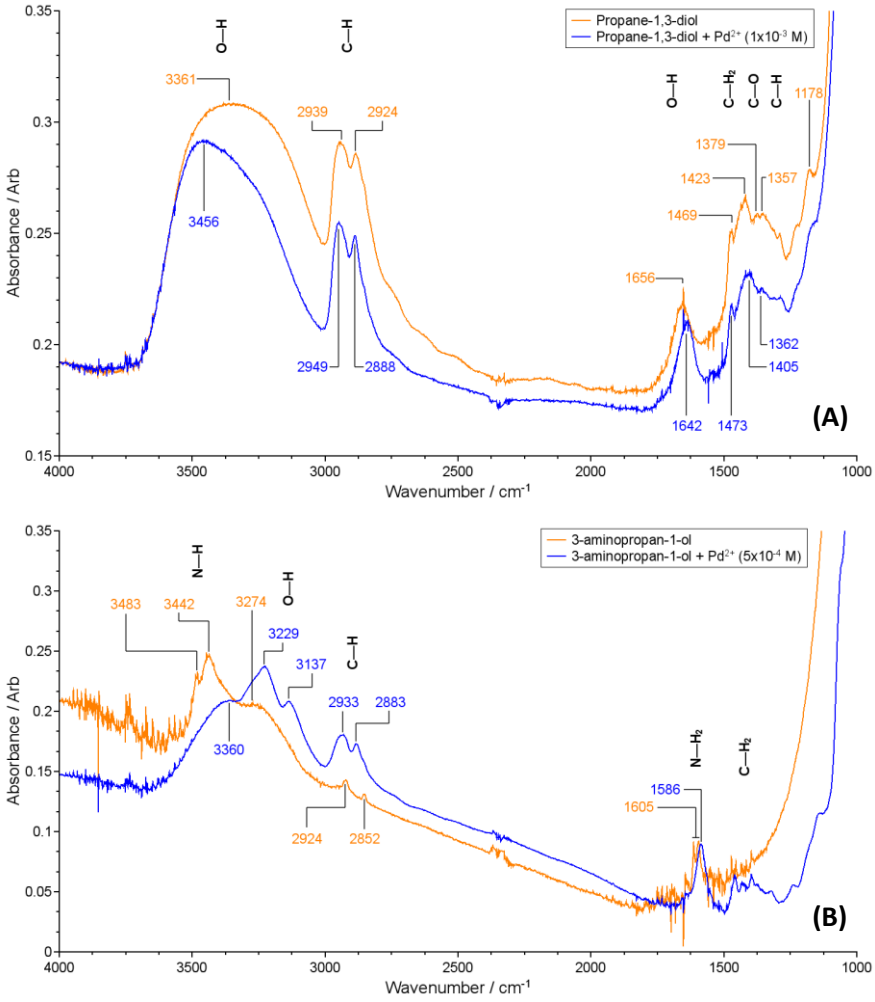

Figure 5. (A) FT-IR spectra of 1,3-propanediol (PD) and Pd-PD (top). (B) FT-IR spectra of 3-aminopropanol (AP) and Pd-AP (bottom).

ions, FT-IR spectra of the Pd(II) complexes were recorded and compared to the FT-IR spectra of the pure ligand molecules, as shown in Figure 5. In the case of propane-1,3-diol, Figure 5 (A), the interaction with Pd^{2+} ions seems to provoke negligible perturbations in the molecular structure of the ligand. Indeed, beside an overall decrease in intensity upon Pd^{2+} addition, only an erosion of the broad peak at 3361 cm^{-1} due to the stretching of –OH groups, together with a shift of the peak related to the –OH bending mode from 1656 cm^{-1} to 1647 cm^{-1} are observed, which indicate that the presence of the Pd^{2+} ions perturbed these groups. This spectroscopic feature points out that the interaction between the metal ions and the propane-1,3-diol ligand occurs through the –OH groups.

Conversely, more significant changes were observed in the FT-IR spectrum of 3-aminopropanol after interaction with Pd^{2+} ions (Figure 5B). The peaks observed at 3483 and 3442 cm^{-1}, related to the symmetric and antisymmetric stretching modes of the -NH group, are decreased and new bands at 3229 and 3137 cm^{-1} are produced immediately upon the addition of Pd^{2+}. Moreover, the -N-H bending mode observed at 1605 cm^{-1} is shifted to 1586 cm^{-1}. To rationalize these differences, in particular, to understand if the peaks at 3229 and 3137 cm^{-1} are the result of a marked shift of the symmetric and antisymmetric stretching modes of the -NH group or of a strong perturbation of the -OH group, frequency calculations were performed in order to simulate FT-IR spectra for the most stable conformations of Pd(II)-AP complex.

Different configurations of the adsorbate were first optimised in the gas phase in order to determine the most stable configuration. Upon optimisation with a plane-wave basis set and the PBE functional, a straight chain configuration and an internally hydrogen bonded conformation (with the hydroxyl oxygen to the amino nitrogen) were found to be the most favourable, with the latter being the most stable. The H-bonded conformation was found to have an electronic energy ~0.8 eV lower than that of the other structure, which was also consistent with results obtained using an atom-centred basis set. The two configurations are shown in figure 6.

These results confirmed the former hypothesis coming from the FT-IR discussion, indicating that the interaction between the metal ions and the 3-aminopropanol ligand occurs through the -NH group. The complete assignments of the FT-IR bands are summarised in Table 3

Table 3: Vibrational frequencies and assignments of the FT-IR bands

Bands observed for 1,3-propanediol	
Vibrational frequency (cm^{-1})	**Assignment (vibrational mode)**
3361	–OH stretching
2939 and 22924	–CH symm and asymm stretchings
1656	–OH bending
1469	$–CH_2$ bending
1423	C-O stretching
1379	C–H bending
Bands observed for Pd-1,3-propanediol	
Vibrational frequency (cm^{-1})	**Assignment (vibrational mode)**
3456	–OH stretching
2949 and 2888	–CH symm and asymm stretchings
1642	–OH bending
1473	$–CH_2$ bending
1405	C-O stretching
1362	C–H bending
Bands observed for 3-aminopropanol	
Vibrational frequency (cm^{-1})	**Assignment (vibrational mode)**
3483 and 3442	–NH symm and asymm stretching
3274	–OH stretching
2924 and 2852	–CH symm and asymm stretchinge
1605	–OH bending
Bands observed for Pd-3-aminopropanol	
Vibrational frequency (cm^{-1})	**Assignment (vibrational mode)**
3360	–OH stretching
3229 and 3137	–NH symm and asymm stretching
2933 and 2883	–CH symm and asymm stretching
1586	–OH bending

For this reason, the interaction of the AP molecule with metallic Pd surfaces was also investigated. The most stable configuration of AP was then adsorbed on the two low index surfaces of palladium metal: Pd (111) and Pd (100). Structures with AP binding to the surface through the oxygen atom or the nitrogen atom were investigated; it was found that those in which both the oxygen and the nitrogen atom bind to the surface at the same time were unstable due to internal strain within the 3-aminopropanol. In the case

with AP adsorbed through the amine N atom, the hydroxyl hydrogen is attracted also towards the surface.

Table 4 and figures 7, 8, 9, and 10 summarise the results obtained.

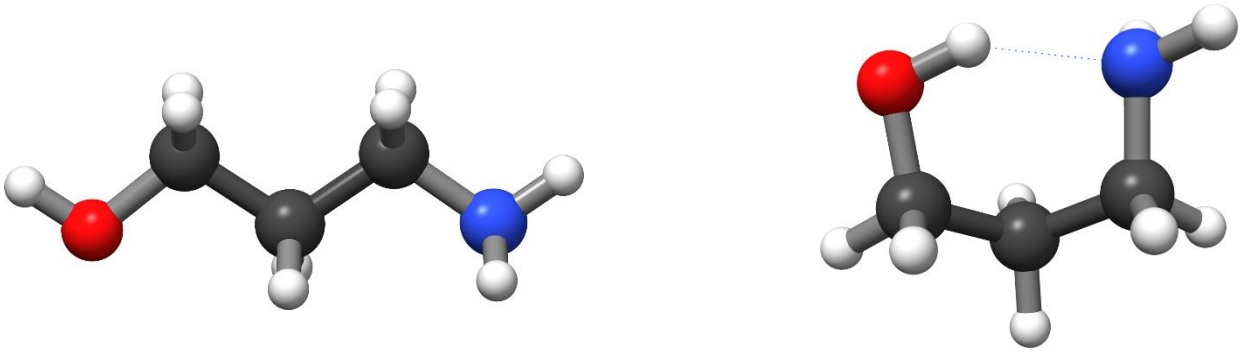

Figure 6: Optimisation of two different conformations of the AP adsorbate in the gas phase: (A) all trans, (B) conformation with internal H-bond

Table 4: Adsorption energies of the different configurations of 3-aminopropan-1-ol on Pd (100) and Pd(111) surfaces

Pd(111) surface		
Configuration	**Energy of Adsorption/ kJ mol^{-1}**	**N-Pd or O-Pd distance / Å**
Nitrogen Binding	-145	2.15
Oxygen Binding	-95	2.34
Pd(100) surface		
Configuration	**Energy of Adsorption/ kJ mol^{-1}**	**N-Pd or O-Pd distance / Å**
Nitrogen Binding (O up)	-127	2.16
Nitrogen Binding (O Down)	-149	2.15
Oxygen Binding	-86	2.32

The conformation with the nitrogen interacting with Pd was found to be more stable on both Pd(111) and Pd(100) surfaces as was also seen for the molecular precursor. Since the Pd(111) surface is more stable than the Pd(100) surface, the bonding of the adsorbate to the Pd(100) surface is stronger. As a result, the ligand is preferentially adsorbed on Pd(100) facets, making the surface less accessible. The reduced accessibility of Pd(100) facets favours the nanoparticles growth on the Pd(111) facet resulting in a greater surface area of Pd(100) facets. This observation confirms the important role of the capping agent in controlling the growth mechanism and directing the final particle shape. In addition, the selective blocking of Pd(100) surface can have an important impact on the catalytic performances of Pd NPs

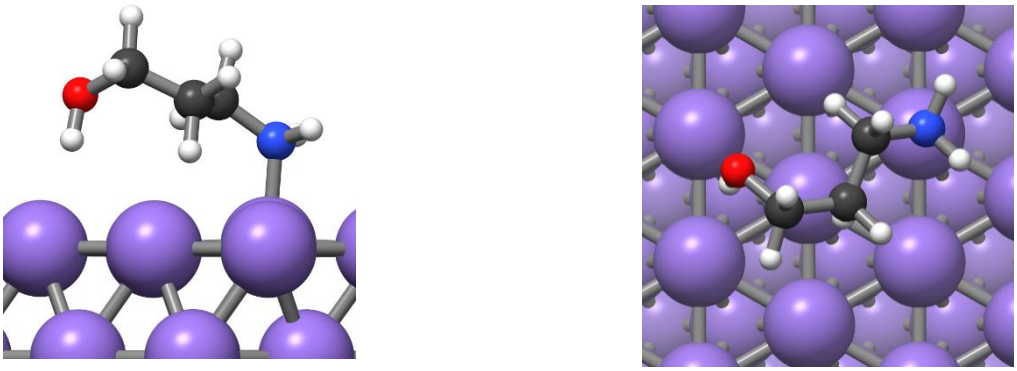

Figure 7: Adsorption of the AP adsorbate on the Pd(111) surface with the nitrogen binding to the surface.

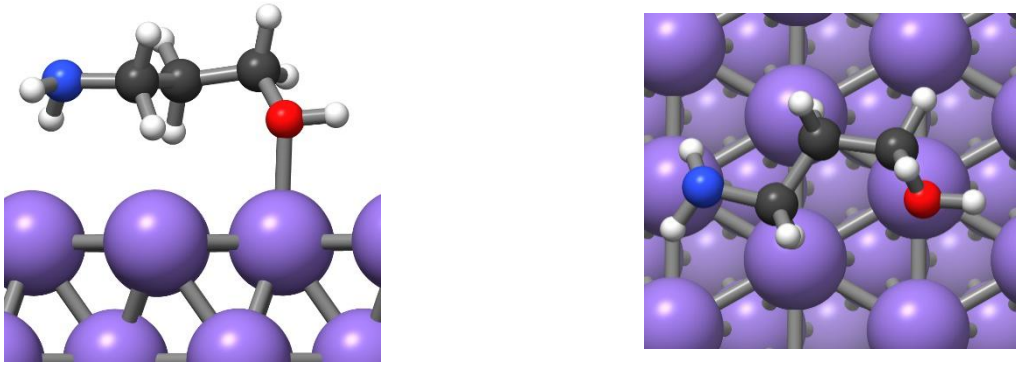

Figure 8: Adsorption of the AP adsorbate on the Pd(111) with the oxygen binding to the surface.

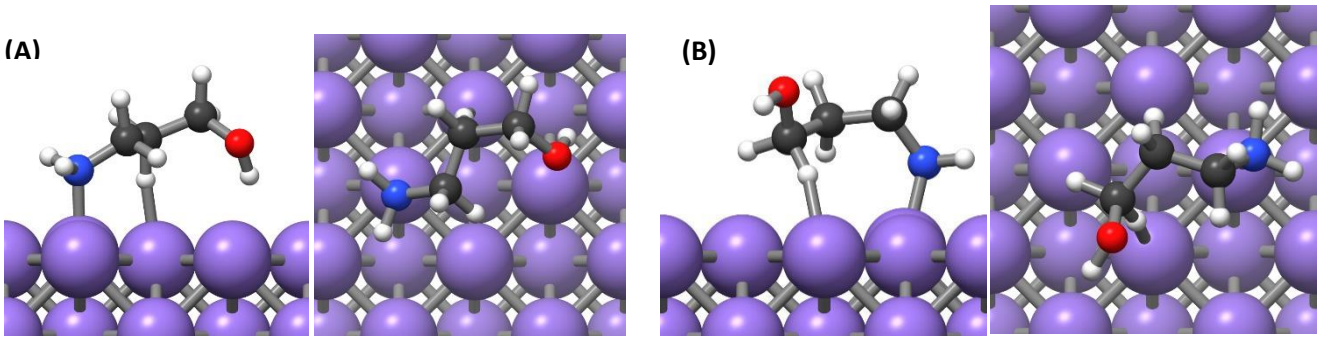

Figure 9: Adsorption of the AP adsorbate on the Pd(100) with the Nitrogen binding to the surface and (A) the oxygen pointing downwards and (B) the oxygen pointing upwards.

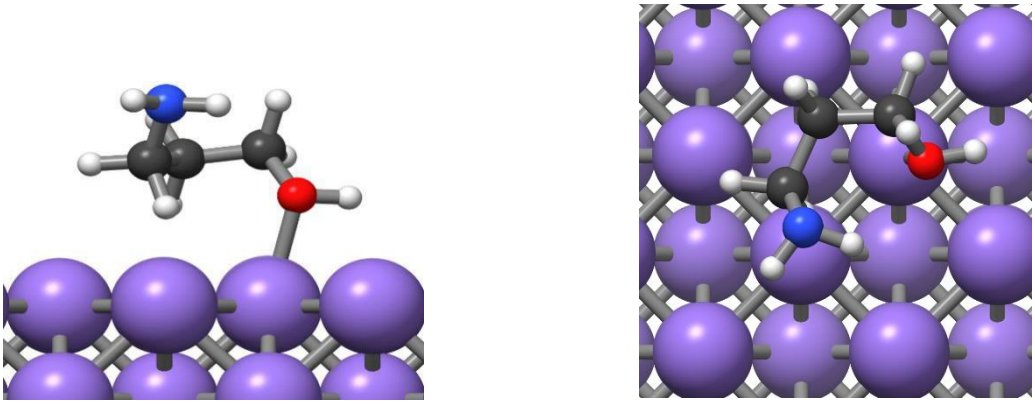

Figure 10: Adsorption of the AP adsorbate on the Pd(100) with the oxygen binding to the surface.

Frequency calculations on the most stable configurations were performed and IR spectra were calculated. The resulting IR spectra for the different conformations are reported in Figure 11. The correlation between the experimental IR spectrum and the spectra obtained for the adsorbed configurations can be taken as a strong indication that the aminopropanol caps the nanoparticle surfaces by bonding through the amino moiety. This is further supported by the oxygen binding spectra which indicate that the O–H vibrational modes are significantly less infrared active than the nitrogen binding O–H modes in both the experimental and computed nitrogen binding spectra. Whilst the accuracy of the extended-surface model for many properties of small NPs is limited, the assignment of the spectrum to the N-binding species should not be of concern. The spectra for the nitrogen binding of AP on the Pd (111) and Pd (100) surfaces are very similar. Given that the difference between the two surfaces is the number of surrounding

atoms, it can be concluded that the coordination number of Pd has very little effect on the vibration energies. Therefore, if the nanoparticles are small to an extent where the corner or edge sites are significant, the adsorption of AP on these sites is not likely to affect the resultant spectra.

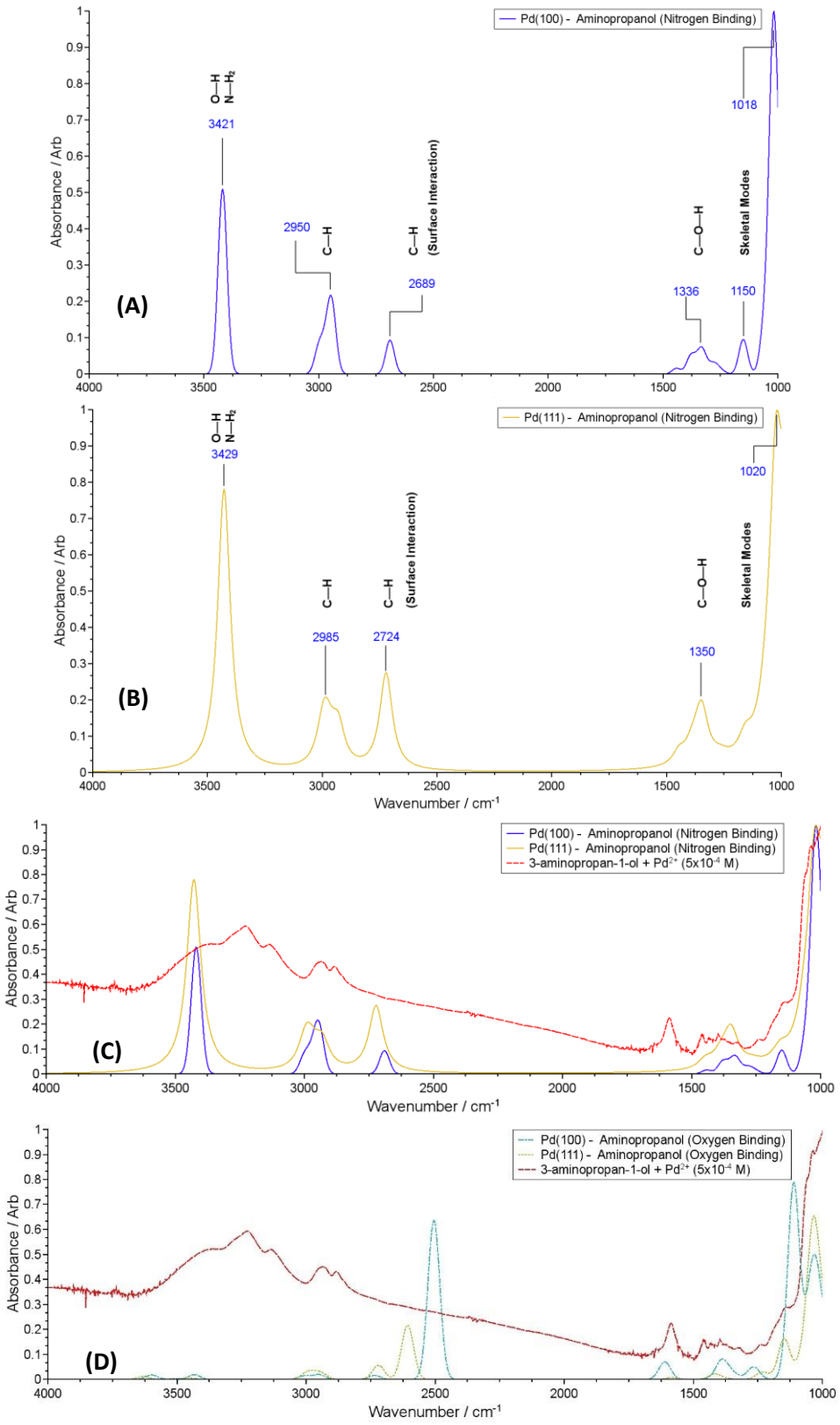

Figure 11: IR spectra for the most stable conformations: (A) Nitrogen binding of the aminopropanol on the Pd (100) surface (B) NItrogen binding of the aminopropanol on the Pd (111) surface (C) Plots A and B overlayed with the experimentally obtained IR spectrum, (D) Oxygen binding on the Pd (111) and Pd (100) surfaces overlayed with the experimentally obtained IR spectrum.

Conclusions

The synergistic combination of experimental spectroscopies and DFT modelling has allowed us to determine the coordination of small ligand to Pd species during metal nanoparticle formation process. Interesting differences emerged between O- and N-containing ligands. In particular, it seems that 3-aminopropanol reacts with the molecular precursors by displacing a chloride ion to form a Pd(II)Cl_3AP complex. AP is able to direct the growth processes during the subsequent reduction by stabilizing the Pd(100) facets and thus exerting a directing influence upon the shape of the resultant metal NPs. Although these molecules are model systems and greater complexity is expected from the adsorption of macromolecules such as polymers, typically used as capping agents, these results help in understanding the phenomena occurring at the interface between the metal surface and the ligand layer. These data will also provide a stimulus to a deeper investigation on the role of capping agent in metal NPs synthesis and in their catalytic behaviour.

Acknowledgements

We acknowledge the support of the Supercomputing Wales project, which is part-funded by the European Regional Development Fund (ERDF) via Welsh Government. Via our membership of the UK's HEC Materials Chemistry Consortium, which is funded by EPSRC (EP/L000202), this work used the UK Materials and Molecular Modelling Hub for computational resources, which is partially funded by EPSRC (EP/P020194).

References

(1) Tao, F. *Metal Nanoparticles for Catalysis: Advances and Applications*; RSC Catalysis Series; Royal Society of Chemistry, 2014.

(2) Capek, I. *Noble Metal Nanoparticles: Preparation, Composite Nanostructures, Biodecoration and Collective Properties*; Nanostructure Science and Technology; Springer Japan, 2017.

(3) Liu, L.; Corma, A. Metal Catalysts for Heterogeneous Catalysis: From Single Atoms to Nanoclusters and Nanoparticles. *Chem. Rev.* **2018**, *118* (10), 4981–5079. https://doi.org/10.1021/acs.chemrev.7b00776.

(4) He, C.; Liu, D.; Lin, W. Nanomedicine Applications of Hybrid Nanomaterials Built from Metal–Ligand Coordination Bonds: Nanoscale Metal–Organic Frameworks and Nanoscale Coordination Polymers. *Chem. Rev.* **2015**, *115* (19), 11079–11108. https://doi.org/10.1021/acs.chemrev.5b00125.

(5) Roldán, A.; Ricart, J. M.; Illas, F. Growth and Properties of Au Nanowires. *Mol. Simul.* **2009**, *35* (12–13), 1051–1056. https://doi.org/10.1080/08927020902902775.

(6) Wu, Y.; Wang, D.; Li, Y. Nanocrystals from Solutions: Catalysts. *Chem. Soc. Rev.* **2014**, *43* (7), 2112–2124. https://doi.org/10.1039/C3CS60221D.

(7) Irzhak, V. I. The Mechanisms of the Formation of Metal-Containing Nanoparticles. *Rev. J. Chem.* **2016**, *6* (4), 370–404. https://doi.org/10.1134/s2079978016040026.

(8) Qi, L.; Castaing, J.; Destremaut, F.; Salmon, J.; Cousin, F.; Chapel, J. Influence of the Formulation Process in Electrostatic Assembly of Nanoparticles and Macromolecules in

Aqueous Solution : The Interaction Pathway. *J. Phys. Chem. C* **2010**, *114* (39), 16373–16381.

(9) Chen, T.; Rodionov, V. O. Controllable Catalysis with Nanoparticles: Bimetallic Alloy Systems and Surface Adsorbates. *ACS Catal.* **2016**, *6* (6), 4025–4033. https://doi.org/10.1021/acscatal.6b00714.

(10) Cargnello, M. Colloidal Nanocrystals as Building Blocks for Well-Defined Heterogeneous Catalysts. *Chem. Mater.* **2019**, *31* (3), 576–596. https://doi.org/10.1021/acs.chemmater.8b04533.

(11) Liu, J.; Legros, S.; Ma, G.; Veinot, J. G. C.; von der Kammer, F.; Hofmann, T. Influence of Surface Functionalization and Particle Size on the Aggregation Kinetics of Engineered Nanoparticles. *Chemosphere* **2012**, *87* (8), 918–924. https://doi.org/10.1016/j.chemosphere.2012.01.045.

(12) Oh, M.; Mirkin, C. A. Chemically Tailorable Colloidal Particles from Infinite Coordination Polymers. *Nature* **2005**, *438* (7068), 651–654. https://doi.org/10.1038/nature04191.

(13) Cortes-Huerto, R.; Goniakowski, J.; Noguera, C. Role of the Environment in the Stability of Anisotropic Gold Particles. *Phys. Chem. Chem. Phys.* **2015**, *17* (9), 6305–6313. https://doi.org/10.1039/C4CP05504G.

(14) Hosseini, S.; Alsiraey, N.; Riley, A. J.; Zubkov, T.; Closson, T.; Tye, J.; Bodappa, N.; Li, Z. Variable Growth and Characterizations of Monolayer-Protected Gold Nanoparticles Based on Molar Ratio of Gold and Capping Ligands. *Langmuir* **2018**, *34* (50), 15517–15525. https://doi.org/10.1021/acs.langmuir.8b02623.

(15) Rode, B. M.; Schwenk, C. F.; Hofer, T. S.; Randolf, B. R. Coordination and Ligand Exchange Dynamics of Solvated Metal Ions. *Coord. Chem. Rev.* **2005**, *249* (24), 2993–3006.

https://doi.org/10.1016/j.ccr.2005.03.032.

(16) Liu, P.; Qin, R.; Fu, G.; Zheng, N. Surface Coordination Chemistry of Metal Nanomaterials. *J. Am. Chem. Soc.* **2017**, *139* (6), 2122–2131. https://doi.org/10.1021/jacs.6b10978.

(17) Ortiz, N.; Skrabalak, S. E. On the Dual Roles of Ligands in the Synthesis of Colloidal Metal Nanostructures. *Langmuir* **2014**, *30* (23), 6649–6659. https://doi.org/10.1021/la404539p.

(18) Costa, N. J. S.; Rossi, L. M. Synthesis of Supported Metal Nanoparticle Catalysts Using Ligand Assisted Methods. *Nanoscale* **2012**, *4* (19), 5826–5834. https://doi.org/10.1039/c2nr31165h.

(19) Varghese, N.; Rao, C. N. R. Journal of Colloid and Interface Science Growth Kinetics of Platinum Nanocrystals Prepared by Two Different Methods : Role of the Surface. *J. Colloid Interface Sci.* **2012**, *365* (1), 117–121. https://doi.org/10.1016/j.jcis.2011.09.005.

(20) Mozaffari, S.; Li, W.; Thompson, C.; Ivanov, S.; Seifert, S.; Lee, B.; Kovarik, L.; Karim, A. M. Ligand-Mediated Nucleation and Growth of Palladium Metal Nanoparticles. *J. Vis. Exp.* **2018**, *31* (136), 1–11. https://doi.org/10.3791/57667.

(21) Yancey, D. F.; Chill, S. T.; Zhang, L.; Frenkel, A. I.; Henkelman, G.; Crooks, R. M. A Theoretical and Experimental Examination of Systematic Ligand-Induced Disorder in Au Dendrimer-Encapsulated Nanoparticles. *Chem. Sci.* **2013**, *4* (7), 2912. https://doi.org/10.1039/c3sc50614b.

(22) Hostetler, M. J.; Wingate, J. E.; Zhong, C.-J.; Harris, J. E.; Vachet, R. W.; Clark, M. R.; Londono, J. D.; Green, S. J.; Stokes, J. J.; Wignall, G. D.; et al. Alkanethiolate Gold Cluster Molecules with Core Diameters from 1.5 to 5.2 Nm: Core and Monolayer Properties as a Function of Core Size. *Langmuir* **1998**, *14* (1), 17–30. https://doi.org/10.1021/la970588w.

(23) Karim, A. M.; Al Hasan, N.; Ivanov, S.; Siefert, S.; Kelly, R. T.; Hallfors, N. G.; Benavidez, A.; Kovarik, L.; Jenkins, A.; Winans, R. E.; et al. Synthesis of 1 Nm Pd Nanoparticles in a Microfluidic Reactor: Insights from in Situ X-Ray Absorption Fine Structure Spectroscopy and Small-Angle X-Ray Scattering. *J. Phys. Chem. C* **2015**, *119* (23), 13257–13267. https://doi.org/10.1021/acs.jpcc.5b01681.

(24) Biacchi, A. J.; Schaak, R. E. The Solvent Matters: Kinetic versus Thermodynamic Shape Control in the Polyol Synthesis of Rhodium Nanoparticles. *ACS Nano* **2011**, *5* (10), 8089–8099. https://doi.org/10.1021/nn2026758.

(25) Mozaffari, S.; Li, W.; Thompson, C.; Ivanov, S.; Seifert, S.; Lee, B.; Kovarik, L.; Karim, A. M. Colloidal Nanoparticle Size Control: Experimental and Kinetic Modeling Investigation of the Ligand–metal Binding Role in Controlling the Nucleation and Growth Kinetics. *Nanoscale* **2017**, *9* (36), 13772–13785. https://doi.org/10.1039/C7NR04101B.

(26) Rossi, L. M.; Fiorio, J. L.; Garcia, M. A. S.; Ferraz, C. P. The Role and Fate of Capping Ligands in Colloidally Prepared Metal Nanoparticle Catalysts. *Dalt. Trans.* **2018**, *47* (17), 5889–5915. https://doi.org/10.1039/C7DT04728B.

(27) Campisi, S.; Schiavoni, M.; Chan-Thaw, C.; Villa, A. Untangling the Role of the Capping Agent in Nanocatalysis: Recent Advances and Perspectives. *Catalysts* **2016**, *6* (12), 185. https://doi.org/10.3390/catal6120185.

(28) Campisi, S.; Ferri, D.; Villa, A.; Wang, W.; Wang, D.; Kröcher, O.; Prati, L. Selectivity Control in Palladium-Catalyzed Alcohol Oxidation through Selective Blocking of Active Sites. *J. Phys. Chem. C* **2016**, *120* (26), 14027–14033. https://doi.org/10.1021/acs.jpcc.6b01549.

(29) Lazzarini, A.; Groppo, E.; Agostini, G.; Borfecchia, E.; Giannici, F.; Portale, G.; Longo, A.;

Pellegrini, R.; Lamberti, C. Formation and Growth of Palladium Nanoparticles inside Porous Poly (4-Vinyl-Pyridine) Monitored by Operando Techniques : The Role of Different Reducing Agents. *Catal. Today* **2017**, *283*, 144–150. https://doi.org/10.1016/j.cattod.2016.06.037.

(30) Abécassis, B.; Testard, F.; Spalla, O.; Barboux, P. Probing in Situ the Nucleation and Growth of Gold Nanoparticles by Small-Angle X-Ray Scattering. *Nano Lett.* **2007**, *7* (6), 1723–1727. https://doi.org/10.1021/nl0707149.

(31) Yin, X.; Shi, M.; Wu, J.; Pan, Y.; Gray, D. L.; Bertke, J. A.; Yang, H. Quantitative Analysis of Different Formation Modes of Platinum Nanocrystals Controlled by Ligand Chemistry. *Nano Lett.* **2017**, *17* (10), 6146–6150. https://doi.org/10.1021/acs.nanolett.7b02751.

(32) Groppo, E.; Agostini, G.; Borfecchia, E.; Wei, L.; Giannici, F.; Portale, G.; Longo, A.; Lamberti, C. Formation and Growth of Pd Nanoparticles inside a Highly Cross-Linked Polystyrene Support: Role of the Reducing Agent. *J. Phys. Chem. C* **2014**, *118* (16), 8406–8415. https://doi.org/10.1021/jp5003897.

(33) Ali, F.; Naseem, K.; Xiao, J.; Irfan, A.; Farooqi, Z. H.; Batool, M.; Begum, R. Applications of UV/Vis Spectroscopy in Characterization and Catalytic Activity of Noble Metal Nanoparticles Fabricated in Responsive Polymer Microgels: A Review. *Crit. Rev. Anal. Chem.* **2018**, *0* (0), 1–14. https://doi.org/10.1080/10408347.2018.1451299.

(34) Bittner, M. M.; Kraus, D.; Lindeman, S. V.; Popescu, C. V.; Fiedler, A. T. Synthetic, Spectroscopic, and DFT Studies of Iron Complexes with Iminobenzo(Semi)Quinone Ligands: Implications for o -Aminophenol Dioxygenases. *Chem. - A Eur. J.* **2013**, *19* (29), 9686–9698. https://doi.org/10.1002/chem.201300520.

(35) Singh, D. K.; Jagannathan, R.; Khandelwal, P.; Abraham, P. M.; Poddar, P. In Situ Synthesis

and Surface Functionalization of Gold Nanoparticles with Curcumin and Their Antioxidant Properties: An Experimental and Density Functional Theory Investigation. *Nanoscale* **2013**, *5* (5), 1882. https://doi.org/10.1039/c2nr33776b.

(36) Ansar, S. M.; Haputhanthri, R.; Edmonds, B.; Liu, D.; Yu, L.; Sygula, A.; Zhang, D. Determination of the Binding Affinity, Packing, and Conformation of Thiolate and Thione Ligands on Gold Nanoparticles. *J. Phys. Chem. C* **2011**, *115* (3), 653–660. https://doi.org/10.1021/jp110240y.

(37) Chen, M.; Feng, Y.-G.; Wang, X.; Li, T.-C.; Zhang, J.-Y.; Qian, D.-J. Silver Nanoparticles Capped by Oleylamine: Formation, Growth, and Self-Organization. *Langmuir* **2007**, *23* (10), 5296–5304. https://doi.org/10.1021/la700553d.

(38) Groppo, E.; Agostini, G.; Borfecchia, E.; Lazzarini, A.; Liu, W.; Lamberti, C.; Giannici, F.; Portale, G.; Longo, A. The Pyridyl Functional Groups Guide the Formation of Pd Nanoparticles Inside A Porous Poly(4-Vinyl-Pyridine). *ChemCatChem* **2015**, *7* (14), 2188–2195. https://doi.org/10.1002/cctc.201500211.

(39) Garcia, M. A.; De La Venta, J.; Crespo, P.; Llopis, J.; Penadés, S.; Fernández, A.; Hernando, A. Surface Plasmon Resonance of Capped Au Nanoparticles. *Phys. Rev. B - Condens. Matter Mater. Phys.* **2005**, *72* (24), 2–5. https://doi.org/10.1103/PhysRevB.72.241403.

(40) Cure, J.; Coppel, Y.; Dammak, T.; Fazzini, P. F.; Mlayah, A.; Chaudret, B.; Fau, P. Monitoring the Coordination of Amine Ligands on Silver Nanoparticles Using NMR and SERS. *Langmuir* **2015**, *31* (4), 1362–1367. https://doi.org/10.1021/la504715f.

(41) Ahner, T. T.; Delissen, F.; Sokolov, S.; Polte, J.; Ahner, T. T.; Delissen, F.; Sokolov, S.; Emmerling, F.; Thünemann, A. F.; Kraehnert, R. Mechanism of Gold Nanoparticle Formation in

the Classical Citrate Synthesis Method Derived from Coupled in Situ XANES and SAXS Evaluation. *J. Am. Chem. Soc.* **2010**, *132* (4), 1296–1301. https://doi.org/10.1021/ja906506j.

(42) Biswas, K.; Varghese, N.; Rao, C. N. R. Growth Kinetics of Gold Nanocrystals: A Combined Small-Angle X-Ray Scattering and Calorimetric Study. *Small* **2008**, *4* (5), 649–655. https://doi.org/10.1002/smll.200700937.

(43) Liao, H.; Niu, K.; Zheng, H. Observation of Growth of Metal Nanoparticles. *Chem. Commun.* **2013**, *49* (100), 11720. https://doi.org/10.1039/c3cc47473a.

(44) Šloufová, I.; Vlčková, B.; Procházka, M.; Svoboda, J.; Vohlídal, J. Comparison of SERRS and RRS Excitation Profiles of [Fe(Tpy) 2] 2+ (Tpy = 2,2':6',2''-Terpyridine) Supported by DFT Calculations: Effect of the Electrostatic Bonding to Chloride-Modified Ag Nanoparticles on Its Vibrational and Electronic Structure. *J. Raman Spectrosc.* **2014**, *45* (5), 338–348. https://doi.org/10.1002/jrs.4468.

(45) Neese, F. The ORCA Program System. *Wiley Interdiscip. Rev. Comput. Mol. Sci.* **2012**, *2* (1), 73–78. https://doi.org/10.1002/wcms.81.

(46) Kresse, G.; Hafner, J. *Ab Initio* Molecular Dynamics for Liquid Metals. *Phys. Rev. B* **1993**, *47* (1), 558–561. https://doi.org/10.1103/PhysRevB.47.558.

(47) Kresse, G.; Hafner, J. *Ab Initio* Molecular-Dynamics Simulation of the Liquid-Metal–amorphous-Semiconductor Transition in Germanium. *Phys. Rev. B* **1994**, *49* (20), 14251–14269. https://doi.org/10.1103/PhysRevB.49.14251.

(48) Kresse, G.; Furthmüller, J. Efficient Iterative Schemes for *Ab Initio* Total-Energy Calculations Using a Plane-Wave Basis Set. *Phys. Rev. B* **1996**, *54* (16), 11169–11186.

https://doi.org/10.1103/PhysRevB.54.11169.

(49) Kresse, G.; Furthmüller, J. Efficiency of Ab-Initio Total Energy Calculations for Metals and Semiconductors Using a Plane-Wave Basis Set. *Comput. Mater. Sci.* **1996**, *6* (1), 15–50. https://doi.org/10.1016/0927-0256(96)00008-0.

(50) Perdew, J. P.; Burke, K.; Ernzerhof, M. Generalized Gradient Approximation Made Simple. *Phys. Rev. Lett.* **1996**, *77* (18), 3865–3868. https://doi.org/10.1103/PhysRevLett.77.3865.

(51) Perdew, J. P.; Burke, K.; Ernzerhof, M. *ERRATA Generalized Gradient Approximation Made Simple [Phys. Rev. Lett. 77, 3865 (1996)]*; 1997.

(52) Blöchl, P. E. Projector Augmented-Wave Method. *Phys. Rev. B* **1994**, *50* (24), 17953–17979. https://doi.org/10.1103/PhysRevB.50.17953.

(53) Kresse, G.; Joubert, D. From Ultrasoft Pseudopotentials to the Projector Augmented-Wave Method. *Phys. Rev. B* **1999**, *59* (3), 1758–1775. https://doi.org/10.1103/PhysRevB.59.1758.

(54) Mark P. Waller, †; Heiko Braun, ‡; Nils Hojdis, ‡ and; Michael Bühl*, †. Geometries of Second-Row Transition-Metal Complexes from Density-Functional Theory. **2007**. https://doi.org/10.1021/CT700178Y.

(55) Grimme, S.; Antony, J.; Ehrlich, S.; Krieg, H. A Consistent and Accurate *Ab Initio* Parametrization of Density Functional Dispersion Correction (DFT-D) for the 94 Elements H-Pu. *J. Chem. Phys.* **2010**, *132* (15), 154104. https://doi.org/10.1063/1.3382344.

(56) Grimme, S.; Ehrlich, S.; Goerigk, L. Effect of the Damping Function in Dispersion Corrected Density Functional Theory. *J. Comput. Chem.* **2011**, *32* (7), 1456–1465. https://doi.org/10.1002/jcc.21759.

(57) Grimme, S. Semiempirical GGA-Type Density Functional Constructed with a Long-Range Dispersion Correction. *J. Comput. Chem.* **2006**, *27* (15), 1787–1799. https://doi.org/10.1002/jcc.20495.

(58) E. F. Valeev. Libint: A Library for the Evaluation of Molecular Integrals of Many-Body Operators over Gaussian Functions. 2018.

(59) Monkhorst, H. J.; Pack, J. D. Special Points for Brillouin-Zone Integrations. *Phys. Rev. B* **1976**, *13* (12), 5188–5192. https://doi.org/10.1103/PhysRevB.13.5188.

(60) Andrae, D.; Häußermann, U.; Dolg, M.; Stoll, H.; Preuß , H. Energy-Adjustedab Initio Pseudopotentials for the Second and Third Row Transition Elements. *Theor. Chim. Acta* **1990**, *77* (2), 123–141. https://doi.org/10.1007/BF01114537.

(61) Weigend, F.; Ahlrichs, R. Balanced Basis Sets of Split Valence, Triple Zeta Valence and Quadruple Zeta Valence Quality for H to Rn: Design and Assessment of Accuracy. *Phys. Chem. Chem. Phys.* **2005**, *7* (18), 3297. https://doi.org/10.1039/b508541a.

(62) Weigend, F. Accurate Coulomb-Fitting Basis Sets for H to Rnw. https://doi.org/10.1039/b515623h.

(63) Grimme, S. A Simplified Tamm-Dancoff Density Functional Approach for the Electronic Excitation Spectra of Very Large Molecules. *J. Chem. Phys.* **2013**, *138* (24), 244104. https://doi.org/10.1063/1.4811331.

(64) Lu, T.; Chen, F. Multiwfn: A Multifunctional Wavefunction Analyzer. *J. Comput. Chem.* **2012**, *33* (5), 580–592. https://doi.org/10.1002/jcc.22885.

(65) Lu, T.; Chen, F. W. Calculation of Molecular Orbital Composition. *Acta Chim. Sin. 69*, 2393–

2406.

(66) Vidossich, P.; Lledós, A. The Use of Localised Orbitals for the Bonding and Mechanistic Analysis of Organometallic Compounds. *Dalt. Trans.* **2014**, *43* (29), 11145–11151. https://doi.org/10.1039/C4DT00251B.

(67) Pipek, J.; Mezey, P. G. A Fast Intrinsic Localization Procedure Applicable for *a b i n i t i o* and Semiempirical Linear Combination of Atomic Orbital Wave Functions. *J. Chem. Phys.* **1989**, *90* (9), 4916–4926. https://doi.org/10.1063/1.456588.

(68) Sit, P. H.-L.; Zipoli, F.; Chen, J.; Car, R.; Cohen, M. H.; Selloni, A. Oxidation State Changes and Electron Flow in Enzymatic Catalysis and Electrocatalysis through Wannier-Function Analysis. *Chem. - A Eur. J.* **2011**, *17* (43), 12136–12143. https://doi.org/10.1002/chem.201101916.

(69) Klasovsky, F.; Claus, P.; Wolf, D. *Influence of Preparation Parameters on the Performance of Colloid-Derived Oxidic Palladium Catalysts for Selective Hydrogenation of C–C Triple Bonds*; 2009; Vol. 52. https://doi.org/10.1007/s11244-008-9173-1.

(70) Wang, H.-F.; Kaden, W. E.; Dowler, R.; Sterrer, M.; Freund, H.-J. Model Oxide-Supported Metal Catalysts – Comparison of Ultrahigh Vacuum and Solution Based Preparation of Pd Nanoparticles on a Single-Crystalline Oxide Substrate. *Phys. Chem. Chem. Phys.* **2012**, *14* (32), 11525–11533. https://doi.org/10.1039/C2CP41459G.

(71) Grogan, M. J.; Nakamoto, K. *Infrared Spectra and Normal Coordinate Analysis of Metal-Olefin Complexes. II. Zeise's Dimer and Its Palladium (II) Analog1*.

(72) Boily, J. F.; Seward, T. M.; Charnock, J. M. The Hydrolysis and Precipitation of Pd(II) in 0.6

Mol Kg-1 NaCl: A Potentiometric, Spectrophotometric, and EXAFS Study. *Geochim. Cosmochim. Acta* **2007**, *71* (20), 4834–4845. https://doi.org/10.1016/j.gca.2007.08.015.